1   **Validity and sensitivity of a human cranial finite element model:**

2   **implications for comparative studies of biting performance.**

3   Running title: Cranial finite element model validation

4   Viviana Toro-Ibacache[1,2], Laura C. Fitton[1], Michael J. Fagan[3], Paul O'Higgins[1]

5   [1] Centre for Anatomical and Human Sciences

6   Department of Archaeology and Hull York Medical School, University of York

7   Heslington, York YO10 5DD

8   United Kingdom

9

10 [2] Facultad de Odontología Universidad de Chile

11 Sergio Livingstone Polhammer 943

12 Independencia, Región Metropolitana

13 Chile

14

15 [3] School of Engineering, Medical and Biological Engineering Research Group

16 University of Hull

17 Hull HU6 7RX

18 United Kingdom

19

20 Address for correspondence:

21 Dr Viviana Toro-Ibacache

22 Facultad de Odontología Universidad de Chile

23 Sergio Livingstone Polhammer 943

24 Independencia, Región Metropolitana

25 Chile

26 Tel: +56 2 29781702

27 Email: mtoroibacache@odontologia.uchile.cl

28

Abstract

Finite element analysis (FEA) is a modelling technique increasingly used in anatomical studies investigating skeletal form and function. In the case of the cranium this approach has been applied to both living and fossil taxa to (for example) investigate how form relates to function or infer diet or behaviour. However, FE models of complex musculoskeletal structures always rely on simplified representations because it is impossible to completely image and represent every detail of skeletal morphology, variations in material properties and the complexities of loading at all spatial and temporal scales. The effects of necessary simplifications merit investigation. To this end, this study focusses on one aspect, model geometry, which is particularly pertinent to fossil material where taphonomic processes often destroy the finer details of anatomy or in models built from clinical CTs where the resolution is limited and anatomical details are lost. We manipulated the details of a finite element (FE) model of an adult human male cranium and examined the impact on model performance. First, using digital speckle interferometry, we directly measured strains from the infraorbital region and frontal process of the maxilla of the physical cranium under simplified loading conditions, simulating incisor biting. These measured strains were then compared with predicted values from FE models with simplified geometries that included modifications to model resolution, and how cancellous bone and the thin bones of the circum-nasal and maxillary regions were represented. Distributions of regions of relatively high and low principal strains and principal strain vector magnitudes and directions, predicted by the most detailed FE model, are generally similar to those achieved *in vitro*. Representing cancellous bone as solid cortical bone lowers strain magnitudes substantially but the mode of deformation of the FE model is relatively constant. In contrast, omitting thin plates of bone in the circum-nasal region affects both mode and magnitude of deformation. Our findings provide a useful frame of reference with regard to the effects of simplifications on the performance of FE models of the cranium and call for caution in the interpretation and comparison of FEA results.

Keywords

Human cranium, finite element analysis, digital speckle interferometry, finite element model validation.

Introduction

Finite element analysis (FEA) is increasingly applied in studies of skeletal form and function. A focus of interest is the craniofacial skeleton where mechanical loading during ontogeny is important in ensuring balanced, normal growth and so, normal adult form and function (Lieberman 1996; Moss 2007; Menegaz et al. 2010). Further, comparative analyses of craniofacial strains predicted by FEA are potentially informative in relation to ecology and diet in both living and fossil taxa (Rayfield 2007; Kupczik et al. 2009; Strait et al. 2009; Wroe et al. 2010; Gröning et al. 2011b; Ross et al. 2011; O'Higgins et al. 2012; Smith et al. 2015b). However, the results of an FEA depend on model geometry, material properties, applied loads and kinematic constraints. Full reproduction of these characteristics in a model of a structure like the human cranium is currently extremely difficult. Among model characteristics, detailed anatomy can be difficult to achieve because of limitations in imaging and thus reconstruction. Representation of anatomy is particularly error prone in the case of fossil material, because of taphonomic alteration of bone internal anatomy (e.g. due to sediment deposition) and tissue characteristics (e.g. similar image characteristics of fossilised bone and sediments) (Turner-Walker and Parry 1995; Olesiak et al. 2010; Fitton et al. 2015), or in the case of models built from clinical computed tomograms where image resolution is limited (Toro-Ibacache et al. 2015). Thus, simplification is inevitably necessary and it is important to assess the validity of FE models and, in particular, to understand how different modelling simplifications impact on performance.

Several studies have assessed FE model validity and sensitivity (Kupczik et al. 2007; Bright and Gröning 2011; Ross et al. 2011; Fitton et al. 2012; Cox et al. 2015; Fitton et al. 2015; Smith et al. 2015a). Collecting *in vivo* strain measurements for validation is impossible in many cases (e.g. because of ethical constraints and in fossils) and, where it is practicable, strain data are usually limited to a few point locations where the siting of strain gauges is feasible. More detailed and comprehensive measurement of surface strains is possible using post mortem material (Gröning et al. 2009) but replicating physiological loading *in vitro* then becomes an issue. In any case, the gathering of experimental data against which FE model performance can be assessed is time consuming, often destructive, subject specific, error prone and only possible in extant, not fossil specimens. A practical solution is to validate one or a limited number of FE models in detail and to base further models on what has been learnt from the validation and accompanying sensitivity analyses. The aim in this scenario is to validate the modelling approach and to understand the sensitivity of

94   models to variants of this approach, with the aims of increasing the accuracy of FE model

95   behaviour and knowing more about the limits of interpretation imposed by simplifications.

96   Several prior studies of FE models of the skull have compared predicted strains with those

97   measured *in vivo* (Strait et al. 2005; Ross et al. 2011), or with strains resulting from loading

98   of wet cadaveric or dried skeletal material (Marinescu et al. 2005; Kupczik et al. 2007;

99   Gröning et al. 2009; Smith et al. 2015a). To our knowledge, only one study to date has

100   validated a model of a human cranium. This used 13 gauges to measure the strains over a

101   cadaveric cranium that was loaded to perform a block-bite using half the dental arch

102   (Szwedowski et al. 2011). The model was built using area-specific linearly elastic and

103   isotropic material properties based on a map of bone density, as well as a hybrid solid-shell

104   mesh, representing cancellous and cortical bone respectively. Sensitivity analyses were

105   performed by varying the elasticity modulus, Poisson's ratio and homogeneous cortical

106   shell thicknesses. The authors showed that the model with the most detailed cortical bone

107   reconstruction and material properties correlated best with the experimental data, however

108   the impact of different simplifications on strain contours and directions was not examined.

109   Among simplification approaches, it is common to omit structures that are very small and

110   not feasible to reproduce accurately at the given model resolution. Such structures include

111   fine plates of bone, cancellous bone, sutures and the periodontal ligaments (Kupczik et al.

112   2007; Wood et al. 2011; Bright 2012). Thus, cancellous bone is often modelled as a bulk

113   material because even relatively large trabeculae are not always distinguishable in computed

114   tomograms (Gröning et al. 2012). Further, in FEA studies of the skull and postcranial

115   skeleton, bone is often allocated simplified homogeneous and isotropic material properties

116   obtained either from the literature or from average values of the specimen itself, rather

117   than by mapping directly measured, heterogeneous orthotropic material properties (Strait et

118   al. 2005; Kupczik et al. 2007) which are often unavailable and, particularly in the case of

119   fossils and living humans, impossible to obtain.

120   Given the need for simplifications in modelling (including the extent to which cortical and

121   cancellous bone are differentiated), the aim of the present study is to provide a frame of

122   reference for the construction of models of the human cranium and those of our

123   anatomically close primate and fossil relatives. Five voxel-based FE models of the same

124   human cranium were built varying their model geometry (anatomical detail and

125   composition). Two manipulations are applied, the first involves changes in anatomical

126   detail that are inevitable when finite element (voxel) sizes vary according to the typical

127   limited range of resolution of primary CT data used in most studies to date, and the second

128   by representing or omitting cancellous bone in the model. To assess the validity of the

129   predictions of the FE models, strains were compared with those measured *in vitro*, in the

130   actual specimen.

131   *In vitro* strains were measured using an optical technique; digital speckle pattern

132   interferometry (DSPI; Yang and Ettemeyer 2003; Yang et al. 2007) which provides a full-

133   field surface measurement of microscopic deformation, from which the surface

134   displacements and strains of an object under load can be calculated. This approach has

135   previously been used to validate predicted stresses and strains from FE models of a human

136   mandible (Gröning et al. 2009) and a pig cranium (Bright and Gröning 2011). It offers

137   several advantages over strain gauges, most notably, DSPI measures strains over the entire

138   field of view, while strain gauges measure them at distinct points.

139   Model sensitivity was assessed by comparing the FEA results among models. Additionally

140   larger, global changes in size and shape of the skull under loading can be compared among

141   model variants using Procrustes size and shape analysis, from geometric morphometrics

142   (Milne and O'Higgins 2012; O'Higgins and Milne 2013). This approach has previously been

143   used in conjunction with strain maps from FEA of skeletal structures (Milne and O'Higgins

144   2012; Fitton et al. 2015). It provides additional insights into modes of global deformation

145   that are useful when assessing the impact of subtle differences among FE models in

146   sensitivity analyses (Gröning et al. 2011a; Fitton et al. 2012; Fitton et al. 2015).

147   The following null hypotheses (H0) were tested:

148   H01: There are no differences in distribution, magnitude and direction between the

149   principal strains predicted by the different FE models, and between these and the principal

150   strains measured *in vitro*.

151   H02: There are no differences in magnitudes and modes of global deformation among the

152   different finite element models.

153   The testing of these hypotheses allows us to assess the magnitude and nature of any

154   differences in performance among the models and between the models and the cadaveric

155   cranium. This consideration leads to some important insights into sources of error and

156   their impact on FEA studies of crania.

157

Materials and methods

Anatomical data

The cadaveric head of a 74 year old man from the repository of the Centre for Anatomical and Human Sciences (Hull York Medical School, HYMS, UK) was used in this study. The subject signed consent for experimental anatomical studies in life, when he donated his remains and ethical approval was obtained from the HYMS Ethics Committee. All experimental work was carried out in accordance with the Human Tissue Act (available at www.hta.gov.uk) and HYMS protocols for the handling and storage of cadaveric material.

The cadaver had been embalmed two years prior to this study using a modified version of the University of Bristol embalming fluid formulation (1.4% formaldehyde and 70% ethanol, Vickers Laboratories Ltd., Pudsey, UK). The head was scanned using computed tomography (CT) at the York Teaching Hospital (York, UK) with a Siemens 16-channel multidetector CT scanner equipped with a STRATON tube (Siemens Somatom Sensation 16, Siemens Healthcare, Erlangen, Germany) at 120 kV and 320 mA with an H60s edge enhancing kernel. Voxel size was 0.48 x 0.48 x 0.7 mm. Initial reconstruction of images was performed using a specialist system (Syngo Multimodality workplace, Siemens Healthcare, Erlangen, Germany) to ensure adequate field of view and image quality. The image stacks were then exported as DICOM files for detailed segmentation and reconstruction as described further below.

In vitro strain measurement.

The head was skeletonised by dissection, removing the soft tissues and the periosteum, taking precautions not to damage the bone surface. The cranium was placed on the platform of a universal material testing machine with a 1 kN load cell (Lloyd's EZ50, Ametek-Lloyd Instruments Inc., Sussex, UK). The position and loading of the cranium was chosen as an easily replicable loading scenario; while the loading was not physiological the loading at the teeth was comparable to the way a tooth is loaded during biting. Steel blocks were used to support the cranium at both mastoid processes and the left central incisor. Compressive vertical forces were applied to the midplane of the frontal squama, 13 mm anterior to bregma (see experimental setup in Fig. 1a). The load was applied in 11 steps of 50 N to achieve a final load of 550 N. The final arrangement of steel supports and load was arrived at by trial and error, with earlier runs of the loading experiment failing due to instability that was corrected by increasing friction between the steel blocks and platform

190   using emery paper. Stability of the cranium after each step was assessed by repeatedly

191   checking that increases in the reaction force at the constrained border of the left central

192   incisor scaled linearly with increasing loads. Five successive and successful experimental

193   rounds (i.e. with stability of the set up and replicable recording of strains and reaction

194   force) for *in vitro* strain measurement in the infraorbital region and four for the frontal

195   process of the maxilla were achieved. The position of the loading point on the cranium was

196   marked to control the position of the load between loading experiments. Incisor reaction

197   forces were measured using a strain meter equipped with a 5 kN load cell (Omega DP25B-

198   S, Omega Engineering Inc., Stamford, USA) previously calibrated by applying known

199   compressive loads with the Lloyd's testing machine described above.

200   Full-field surface strains were measured using a Q-100 DSPI system (DANTEC Dynamics

201   GmbH, Ulm, Germany). The regions selected for strain measurement in this study were

202   the left infraorbital area and the frontal process of the maxilla, since both show high strains

203   in FEAs of simulated incisor bites in primates (Gross et al. 2001; Kupczik et al. 2009;

204   Fitton et al. 2012). This system provides a maximum field of view (FOV) of 25 x 33 mm^2.

205   The measured surfaces were covered with a thin layer of white spray (DIFFU-THERM

206   developer BAB-BCB, Technische Chemie KG, Herten, Germany) to prevent surface

207   reflection of ambient light. The Q-100 sensor was glued using its three legs to the

208   boundaries of the treated surface using an acrylic-based adhesive (X60, HBM Inc.,

209   Darmstadt, Germany). Sensor attachment to the surface is standard procedure in using the

210   Q-100 system for safety critical engineering work. While there is a theoretical impact on

211   measured strains, in practice any effect is restricted to close to the points of attachment

212   which were not included in the analyses. This procedure was undertaken once for each

213   surface, thus avoiding variations in the location of the measured surface between loading

214   runs. Surface characterisation, phase calculation and deformation estimation (see steps in

215   Fig. 1b) were carried out using the Istra Q-100 (v.2.7, DANTEC Dynamics GmbH, Ulm,

216   Germany). The primary strain data produced by the Q-100 system, maximum (ε_1) and

217   minimum (ε_3) principal strain magnitudes, plus 2D and 3D colour-coded strain contour

218   plots (representing strain distributions, i.e. relative locations of high and low strain) were

219   exported and used for comparison of FEA results.

220   **FE model construction**

221   The cranium was reconstructed from the CT images through a combined approach of

222   thresholding and manual segmentation of bone and teeth using the visualisation program

223   Avizo (v.7.0.1, Visualization Sciences Group, Burlington, USA). Five different models were

224   built (Table 1). To assess the impact of simplifying cancellous bone representation, in one

225   model (model 1) cancellous bone was omitted, and hence all bone was modelled as a solid

226   material with the Young's modulus of cortical bone. This approach has been used in

227   previous studies of cranial FE models (Wroe et al. 2010; Bright and Gröning 2011; Fitton

228   et al. 2012; Jansen van Rensburg et al. 2012; Toro-Ibacache et al. 2015) and is particularly

229   relevant in cases where, because of model resolution, fossilisation and taphonomic

230   processes, or in order to generate hypothetical model geometries via surface warping,

231   modelling cancellous bone is impractical (Bright and Gröning 2011; O'Higgins et al. 2011;

232   Fitton et al. 2015). The remaining models (models 2-5) have a cortical shell with cancellous

233   bone defined as a bulk material of much lower modulus than cortical bone, approach also

234   used in previous studies (Kupczik et al. 2009; Smith et al. 2015a). In these four remaining

235   models, cancellous bone was represented as a bulk material in the regions normally strained

236   during FE biting simulations, below the level of the fronto-zygomatic suture, including the

237   anterior and middle portions of the cranial base.

238   The inner walls of the frontal, ethmoidal, sphenoidal and maxillary sinuses are often

239   thinner than a single voxel and so are prone to being incompletely and poorly represented

240   in the CT. In consequence, the question arose as to how best to represent them in an FE

241   model. To assess the impact of omitting or including them in the model their anatomies

242   were either fully reconstructed manually, albeit using one or two voxels to represent their

243   thickness, or left as assigned by grey level thresholding, resulting in thin plates of bone with

244   irregular holes. Model resolution was varied via resampling by using two different voxel

245   sizes (0.48 mm and 0.35 mm) to simulate the effect of typical differences in resolution in

246   CT scans used in previous FE studies of crania. Reducing voxel size achieves a more

247   accurate representation of the thin inner nasal walls compared to using the larger voxel

248   size. It is of interest to assess the effect of such differences between corresponding models

249   (models 2 vs. 4 and 3 vs. 5). We were unable to carry out a more detailed convergence

250   analysis comparing a range of mesh resolutions because of limitations of resolution of the

251   clinical CT scanner in relation to the finest details of bony anatomy.

252   Anatomical details were refined manually in each model where needed, thus varying the

253   total number of voxels and so, elements among models. In all cases, teeth were modelled as

254   one material with a higher elastic modulus (E) than bone. The characteristics of each model

255   are detailed in Table 1 and their features are depicted in Fig. 2a. Subsequently, data were

256   exported as BMP stacks and converted into FE meshes of eight-noded linear cubic

257   elements by direct voxel conversion. Model pre- and post-processing were performed using

258   the custom FEA program VOX-FE (Fagan et al. 2007; Liu et al. 2012).

259   In all models cortical bone, cancellous bone and teeth were allocated homogeneous linearly

260   elastic and isotropic material properties (with Poisson's ratio=0.3), following the approach

261   used in previously validated models of human and macaque crania (Kupczik et al. 2007;

262   Szwedowski et al. 2011) and the human mandible (Gröning et al. 2009). In models 2-5,

263   cancellous bone was represented as a different material and was allocated an E of 56 MPa

264   (Misch et al. 1999) and an E of 50 GPa was assigned to teeth, this being approximately the

265   mean of the large range of values found in the literature for enamel and dentine (Meredith

266   et al. 1996; Barak et al. 2009; Benazzi et al. 2012). The material properties of cortical bone

267   are particularly important in relation to overall model stiffness (Marinescu et al. 2005; Strait

268   et al. 2005) and these vary throughout the cranium. For this reason material properties of

269   the cadaveric cranium were measured directly from two different regions before settling on

270   a suitable uniform value. A bone sample was collected from the maxillary tuberosity and

271   from the zygomatic arch. E was measured using a nano-hardness tester with a Berkovitch

272   diamond indenter (CSM Instruments SA, Peseux, Switzerland) following the protocol in

273   Kupczik et al. (2007). The average value was found to be 16.3±3.7 GPa for the tuberosity

274   and 21.9±2.7 GPa for the zygomatic arch. Since these values lie within the range used in

275   the literature for models of the human cranium (Horgan and Gilchrist 2003; Wroe et al.

276   2010; Jansen van Rensburg et al. 2012), a single E of 17 GPa, which has been used in

277   previous models (Kupczik et al. 2009; Gröning et al. 2011b; Fitton et al. 2012), was

278   assigned to all cortical bone.

279   The points of applied vertical load, the biting point and mastoid support were replicated in

280   the model. The predicted bite force in model 5 was used to check the loading condition by

281   confirming that this matched the reaction force measured *in vitro* at the left upper incisor.

282   Based on the experimental setup and to simulate loading conditions (i.e. vertically loaded

283   incisor and immobilised mastoids), a vertical kinematic constraint was applied to the tooth,

284   and constraints in all three-axes at each mastoid process. Loads and constraints were

285   applied to the model in the form of selected nodes in the border of the incisor, and

286   punctiform regions of nodes at the point of load application and tips of the mastoid

287   processes.

288   **Measured vs. predicted strains**

289   The procedure to compare strains measured *in vitro* and those predicted by the FE models

290   comprised three steps: (1) matching the FOV of the DSPI with the area of interest of the

291   FE model, (2) data extraction and (3) data comparison.

292   To compare visually strain contours (representing strain distribution) similar colours were

293   mapped to equivalent strain ranges from DSPI and FEA. The surface geometry of the

294   region of the face measured by DSPI was exported as a Virtual Reality Modeling Language

295   (VRML) file and visualised in 3D using Avizo. The surface of the cranium extracted from

296   the CT was loaded into the same scene as the DSPI surface. The DSPI surface was then

297   manually positioned to obtain the best fit with the cranium surface guided by anatomical

298   structures and high magnification photographs of the skull surface. Best-fit was assessed by

299   two observers (VT-I and PO). Coordinates marking the location of the DSPI surface on

300   the CT-derived cranial surface were saved using Avizo in order to match the positions of

301   sampling points among models.

302   The strain magnitude outputs form DSPI and FEA are not the same in both dimensionality

303   (2D for DSPI and 3D for FEA) and resolution, making one-to-one comparison

304   impossible. We therefore used an approach that compares profiles of strain magnitudes

305   along corresponding lines traced over the surfaces of the specimen and model. The DSPI

306   computes strain magnitudes over a regular 2D grid in the plane of the lens. Two straight

307   lines in this plane (lines 1 and 2) were traced across the infraorbital and two across the

308   frontal process fields of view (FOV; lines 3 and 4) using the vertices of the FOVs to

309   optimise replicability of measurement. Line correspondence between the models and the

310   DSPI surfaces is shown in Figs. 3a and 3b. Strain magnitudes at each point along the lines

311   from DSPI were extracted and smoothed by once-averaging of singe adjacent points on

312   either side to reduce noise. To extract corresponding data from the 3D surface of the FE

313   model, lines of landmarks were traced on the model surface forming equivalent straight

314   lines to those used to extract strain magnitudes from the DSPI FOVs. Lines comprising 37

315   (line 1), 30 (line 2), 28 (line 3) and 33 (line 4) landmarks were traced over the model in

316   Avizo. These lines replicate those traced on the DSPI FOVs but they inscribe curves over

317   the surface of the FE model. These curves have two dimensions, distance and depth, while

318   DSPI traced lines have just one dimension, distance. The depth dimension was removed

319   from each FE model curve by projecting it onto the plane described by its first two

320   principal components. The first principal component, which represented distance rather

321   than depth, was then rotated into the plane of the DSPI FOV to achieve best fit. The strain

322   values were smoothed in VOX-FE by once-averaging of neighbouring voxels in order to

323   reduce strain fluctuations due to voxellation (Liu et al. 2012). After smoothing, predicted

324   strain magnitudes at each of the landmarks were extracted for comparison against strains

325   measured *in vitro*. The impact of simplifications of the model on relative (rather than

326   absolute) strain magnitudes was assessed by calculating the correlation coefficient among

327   models.

328   Both systems output surface strain magnitudes and vectors, the Istra Q-100 (DSPI) in 2D

329   and VOX-FE in 3D. These software tools show vectors differently; with directions and

330   magnitudes being represented in the VOX-FE output and directions alone in the Istra Q-

331   100 outputs. Further, the densities and spacings of plotted vectors differ between the

332   visualisations. Thus, to avoid crowding, in the visualisations from VOX-FE lines

333   representing strain vectors were drawn at every fourth node in models 1, 2 and 3 and at

334   every eighth node in the larger models, 4 and 5, over the areas of interest.

335   **Global model deformation**

336   It is important to note that there are two different definitions of the term 'deformation'. In

337   material science and in the context of morphometrics, 'deformation' refers to changes in

338   size and shape (local or global). This is the definition followed here since it reflects the

339   quantities measured by strains, i.e. how the finite elements deform under load. This differs

340   from the definition of 'deformation' used occasionally in mechanics (see Truesdell and Noll

341   2004, p.48) where it may refer to the displacement of nodes of the FE model between

342   unloaded and loaded states.

343   Global model deformations (changes in size and shape) resulting from applied loads were

344   compared between FE models through Procrustes size and shape analyses based on 51

345   craniofacial landmarks (described in Table 1, Supporting information) and visualised in Fig.

346   3c). During size and shape analysis, coordinates are rotated and translated, thus preserving

347   the changes in model size as well as shape due to loading. The resulting size and shape

348   coordinates are then submitted to principal components analysis (PCA; O'Higgins et al.,

349   2012; Fitton et al., 2015). Visualisations of predicted changes in cranial size and shape due

350   to loading and the differences in modes of deformation among models used the surface

351   corresponding to model 1, warped to the mean unloaded landmark configuration before

352   further warping to represent model deformations. Two Cartesian transformation grids were

353   drawn over the mean landmark configuration, and warped with the surface to facilitate

354   interpretation of visualised deformations (Fitton et al. 2012; O'Higgins et al. 2012). Since

355   landmarks are placed only once on the CT-derived surface representing all the models,

356   there is no measurement error associated to the method.

357

358   **Results**

359   The experimental setup was replicated in VOX-FE for each of the models 1-5. The

360   locations of each constrained point and applied load, plus the predicted vs. actual bite force

361   measured *in vitro* were used to achieve accurate model and load orientation. The

362   experimentally measured bite force in the most anatomically accurate model, 5, was

363   176.84$\pm$9.44 N and the predicted bite force was 177.11 N. Repeating this setup, model 4

364   predicted 177.21 N of bite force, whereas low-resolution models 1, 2 and 3 predicted 182,

365   182.54 and 182.55 N of bite force respectively.

366   The results of the strain and global model deformation analyses are presented below.

367   **Measured vs. predicted strains**

368   In general, the strain contour plots predicted by the FEAs differ among models in

369   magnitude but show similar distributions of regions of relatively high and low strain (Figs.

370   2b, and 2c with adjusted strain ranges to improve visualisation). This is also evident from

371   the plots of strain magnitudes (Figs. 4 and 5) where strains from the FE simulations are

372   compared with the *in vitro* ranges. The match is better for lines 1 and 2 than for lines 3 and

373   4. By comparing models 1, 2 and 4 with model 5, it appears that the main effect of

374   representing regions of cancellous bone as solid cortical bone and reconstructing sinus and

375   nasal walls was to increase model stiffness. Comparing FE models with each other and

376   with the results from DSPI, the 'solid' model 1 shows strains three to four times lower than

377   the *in vitro* results and the strains predicted for the other models (Figs. 4 and 5). Overall,

378   models 2 to 5 showed similar strain magnitudes. However, models 2 and 4 (with

379   incompletely reconstructed sinus and nasal walls) show the largest discrepancy with the

380   values measured *in vitro* (particularly ε_3 values; Fig. 5) and the lowest correlations (Table 2)

381   with model 5 of strains traced along the lines drawn over the frontal process of the maxilla

382   (see Figs. 3a and 3b). Model resolution (comparing models 2 vs. 4 and 3 vs. 5) over the

383   limited range assessed in this study does not have an effect on strain magnitude.

384   There are some differences in strain magnitudes between models and the experimentally

385   measured strains, and between models 1, 2 and 4 compared to model 5 (the most accurate).

386   However, the directions of the principal strain vectors are very consistent among models.

387   These mainly consist of vertical compression and transverse tension of the nasal notch

388   (Fig. 6) and of the infero-medial margin of the orbital opening in the frontal process of the

389   maxilla (Fig. 7). This is evident despite the differences described earlier in the ways strain

390   vectors are displayed in the DSPI and VOX-FE outputs.

391   **Global model deformation**

392   The PCA of size and shape variables confirms and clarifies the findings from the analyses

393   of strains with regard to differences and similarities in modes of deformation. In the plots

394   of principal components (PCs), model deformations are represented by lines connecting

395   the loaded and unloaded models (Fig. 8). Global deformations generally consist of dorso-

396   ventral bending of the maxilla mainly at the level of the nasal notch. The deformations of

397   models 1, 3 and 5 are virtually the same in direction (mode of deformation), varying only in

398   magnitude with model 1 deforming less. Models 2 and 4 deform to greater degree and in

399   subtly different ways from the others, with more vertical compression of the nasal aperture

400   and lateral displacement of the mid to upper parts of the nasal margins. They also deform

401   more asymmetrically than the other models. The magnitudes of model deformation due to

402   loading are very small. As such, to aid visualisation the warpings in Fig. 8 were magnified

403   250 times.

404

405   **Discussion**

406   The aim of the present study was to validate the performance of FE models of a human

407   cranium and to assess their sensitivity to variations in anatomical detail and, secondarily, in

408   model resolution. This is important because finite element models of crania are increasingly

409   used to assess and compare function.

410   For this, a wet cadaveric human cranium was loaded experimentally, simulating a bite at the

411   left upper incisor and the resulting strains and reaction force at the incisor were measured.

412   These were then compared to the strains predicted by FE models built using two different

413   simplification approaches: presence or absence of cancellous bone and inner sinus and

414   nasal walls, and high or low resolution. It was hypothesised that there are no differences in

415   distribution, magnitude and direction between the principal strains predicted by FE models

416   built using different segmentation approaches, and between these and the principal strains

417   measured *in vitro*.

418   Bite forces were measured during the loading experiments and the predicted bite force was

419   obtained from each model after loading. The vector of the load applied to the

420   neurocranium was adjusted until the bite force predicted in model 5 matched the force

421   measured *in vitro*. A change in 0.1° in load orientation (or skull orientation) produced a

422   difference of about 1 N in predicted bite force. The predicted bite forces from the lower

423   resolution models were up to 3% higher when the same loads and constraints were applied

424   to them, presumably reflecting subtle differences in how the applied load is transferred to

425   the constraints when model resolution is reduced.

426   Model sensitivity to varying construction approaches was assessed in terms of strain

427   magnitudes, contour plots and principal strain vector orientations. To date, this study

428   presents the largest full field surface strain measurement and comparison carried out on a

429   cranium. Additionally a Procrustes size and shape analysis compared global deformations

430   among models.

431   The results of experiments conducted to test the hypotheses and considerations with

432   regard to the use of simplifications when building FE models of the human cranium are

433   discussed below.

434   **Measured vs. predicted strains**

435   This study used a voxel-based approach for FE mesh generation that is fast and automated,

436   facilitating the process of model construction (Keyak et al. 1990; Lengsfeld et al. 1998).

437   The results show that, irrespective of model geometry and resolution, the FE models

438   predict strain distributions (i.e. distribution of regions of relatively high or low strain) that

439   are similar to those measured in the cranium under experimental loading. The main

440   differences are in strain magnitudes; with the results from models with cortical and

441   cancellous bone represented separately being closest to the values measured *in vitro*. Among

442   these models, those with careful reconstruction of sinus and nasal walls showed the best

443   overall fit to *in vitro* data. This is expected; anatomically more accurate FE models behave

444   more similarly to the real cranium under experimental loadings than do simplified models

445   (Marinescu et al. 2005; Strait et al. 2005; Kupczik et al. 2007). In the frontal process of the

446   maxilla, ε_1 strains of models 2 and 4 better match the *in vitro* strain magnitudes than the

447   remaining models, but only for a part of the traced line lengths. ε_3 strains in models 2 and 4

448   differ from the *in vitro* range (Fig. 5). The strain magnitudes along the traced lines (on Fig.

449   3a) show the lowest correlation with model 5 for models 2 and 4 (Table 2). These results

450   reflect an issue in model building where the sinus and nasal walls are thinner than the width

451   of a voxel. By excluding the walls, the model is more flexible; for ε_1 this results in a closer

452   match in parts but for ε_3 a worse match than if the walls are reconstructed. This problem of
453   how to represent very thin structures in low resolution models has no clear solution.
454   However the models with reconstructed sinus and nasal walls generally perform more
455   reliably than those without, and hence reconstructing them, even though they appear
456   thicker than they are in reality, would be a reasonable way to address this problem.

457   In model 1 where cancellous bone is represented as a solid material with properties of
458   cortical bone, strains were on average about 3.5 times lower than in the more detailed
459   models. Thus, not including cancellous bone as a low modulus distinct material produces a
460   significant increase in model stiffness. However, surface strain distributions (rather than
461   magnitudes) in the contour maps remain approximately consistent among all models (1, 3
462   and 5) with reconstructed sinus and nasal walls. This is more evident when the contour
463   plots of these three models are scaled individually to use a similar range of the colour map
464   (Fig. 2c). These results parallel those of (Fitton et al. 2015) and support the use of the
465   simplification approaches used here if *relative* rather than *absolute* magnitudes of strains are
466   of interest since they have limited local impacts on strain contours. The reduction in strains
467   due to stiffening of the cancellous bone material between models reflects the findings of
468   Renders et al. (2011) who noted a reduction in stresses with increasing trabecular mineral
469   density heterogeneity in study of bone from the mandibular condyle. These findings are of
470   importance in FEA studies where accurate representation of cancellous bone or sinus and
471   nasal walls is not possible such as in fossils or damaged archaeological material or where
472   the construction of high resolution models is impractical. However, attention should be
473   paid when comparison is made among individuals of significantly different sizes, where
474   there is a possibility that the distribution of cancellous bone differs allometrically (i.e. larger
475   individuals having disproportionately more extensive areas of cancellous bone and vice
476   versa), potentially impacting on modes of deformation (Chamoli and Wroe 2011).

477   Model resolution, over the limited range assessed here, has no appreciable effect on model
478   performance, and suggests that the model is close to convergence in the areas investigated.
479   However, since there was no CT scan with a higher resolution available, increasing model
480   resolution in this study was effected by increasing element number, this may not accurately
481   replicate the true differences in resolution of scan data.

482   The effect of another parameter of importance in FEA, material properties, was not
483   considered in this study although it is known that cranial skeletal material properties are
484   heterogeneous (McElhaney et al. 1970; Dechow et al. 1993; Peterson and Dechow 2003;

485   Schwartz-Dabney and Dechow 2003). The use of linearly elastic, isotropic material

486   properties of bone homogeneously throughout the skull is common in FEA (Kupczik et al.

487   2009; Wroe et al. 2010; Bright and Gröning 2011; Gröning et al. 2012). Using

488   heterogeneous material properties improved model accuracy in a study by Strait et al.

489   (2005), but this required a large amount of preliminary work in mapping and representing

490   heterogeneity and it considerably increased model complexity to achieve solution.

491   Moreover, determination of material properties is impossible in fossil material and

492   impractical in studies based on medical CTs from living individuals, which are usually of

493   too low a resolution to allow accurate material property determination based on Hounsfield

494   units. However, several validation and sensitivity analyses support the use of simplified,

495   homogeneous, material properties throughout the skull, since such models achieved results

496   reasonably close to experimental data (Strait et al. 2005; Kupczik et al. 2007; Gröning et al.

497   2009; Szwedowski et al. 2011). The empirical findings of the present study indicate that

498   using linearly elastic, isotropic and homogeneous material properties for the cranium and

499   teeth, results in good concordance between predicted and measured strain contours when

500   the sinus and nasal walls are represented in the model. However this depends on accuracy

501   in representing model geometry, in replicating the experimental loading conditions, and on

502   the choices made with regard to material properties. In the present study we directly

503   measured E in two locations, the maxillary tuberosity ($E = 16.3\pm3.7$ GPa) and the

504   zygomatic arch ($E = 21.9\pm2.7$ GPa). It turned out that using an intermediate value,

505   achieved strain magnitudes that reasonably matched measured ones, but other values for E

506   could also have been chosen and the choice of homogenous, isotropic material properties

507   is arguably a source of error that would tend to make the model more or less flexible

508   (affecting magnitude rather than mode of deformation). In this regard it is worth noting

509   that, in a study in which material properties of a macaque skull were varied, Berthaume et

510   al. (2012), found that 'large variations in modest-to-high *strains* and lower variations in

511   modest-to-high *stresses* occur due to variation in material property values'. Thus, beyond

512   the impact of simplifications of the FE model described here, errors in allocation of

513   material properties also produce errors and so uncertainties with regard to estimated

514   strains. The sum of such errors could potentially have a significant impact on, and limit,

515   comparative studies of cranial biting performance. Further, Daegling et al. (2015) found

516   that there is significant individual variation of material properties in the mandible, such that

517   to incorporate them in a specific model, requires specimen specific measurement.

518   However, we achieve a good match between strains in our most detailed homogenous,

519   isotropic model and those measured experimentally. Given that errors in material property

520   allocation can have a marked effect, and that specimen specific data are not readily acquired

521   (although they can be approximated directly from CT density) it seems reasonable to prefer

522   simplified homogenous isotropic properties when accurate and detailed specimen specific

523   data are not available.

524   Considering all of these results, model construction using simplification approaches that

525   preserve sinus and nasal wall anatomy such as those described here (models 1, 3 and 5)

526   does not appear to impact greatly on mode of deformation. However, variations in

527   predicted strains among these models indicate that accurate estimates of strain magnitude

528   are more difficult to achieve. It is only because we have experimental validation data that

529   we have confidence in these predicted strain magnitudes. With fossils or in circumstances

530   where experimental validation is impossible predicted strain magnitudes will suffer from

531   error of unknown degree. Does this mean that prediction of cranial deformation is not

532   possible without prior validation? A consideration of global deformations is informative in

533   this regard.

534   **Global model deformation**

535   In terms of global deformation, it is apparent that model sensitivity to how the internal

536   sinus and nasal walls are reconstructed differs from and has greater overall impact than

537   sensitivity to the presence of cancellous bone or variations in model resolution. Thus in the

538   PC plot of Fig. 8 the three models (models 1, 3 and 5) with reconstructed sinus and nasal

539   walls deform very similarly (direction of vector connecting unloaded and loaded models),

540   differing mainly in the magnitude of deformation (length of vector connecting unloaded

541   and loaded models). These deform differently (direction and magnitude) to models in

542   which the sinus and nasal walls are omitted (models 2 and 4). These models manifest a

543   higher degree and somewhat different modes of dorso-ventral maxillary bending. This

544   contrasts with the effects of not representing cancellous bone as a separate material (model

545   1 vs models 3 and 5), where the major impact is on the magnitude (vector length) rather

546   than mode (vector direction) of deformation. Model resolution when varied over the range

547   assessed in this study has little effect among models 3 and 5, whereas between models 2

548   and 4, without inner sinus and nasal walls, the difference between models is comparatively

549   larger.

550   It should be borne in mind that the PCA of size and shape offers quite a different insight
551   into model performance than analyses of stresses and strains. Thus, Procrustes size and
552   shape analyses of global deformations describe general features of deformation such as
553   dorso-ventral bending or twisting (O'Higgins et al. 2012) while stresses and strains are
554   relevant to prediction of failure/fracture and possibly, remodelling activity.

555   **Wider considerations**

556   It should be noted that the physical cranium was loaded non-physiologically because of
557   practical constraints, but the FE models were loaded identically to allow comparison. Of
558   course, our findings may differ from those that would have arisen from physiological
559   loading. For instance, the zygomatic region is relatively unstrained in our study, whereas it
560   shows high strains in experimental and modelling studies (Strait et al. 2009; Bright and
561   Gröning 2011; Berthaume et al. 2012; Fitton et al. 2015) and lower strains when the
562   masseter muscle is deactivated (Fitton et al., 2012). This said, the extent to which these
563   findings of high zygomatic region strains reflect reality has been questioned by Curtis et al.
564   (2011), who found that inclusion of temporal fascia in an FE model of a macaque greatly
565   reduced strains in this region. Beyond this limitation, only one loading scenario, at a single
566   bite point has been assessed. Both the non-physiological and limited loading scenarios used
567   in this study may well lead to its findings not reflecting the full complexity and detail of
568   differences among modelling approaches and between these and the physical cranium. This
569   should be borne in mind when generalising from the present findings.

570   Using diverse approaches to comparing FE model performance (strain contour maps,
571   strain vector magnitudes and directions, and global model deformation), we have
572   demonstrated that simplifications in model geometry and material properties impact on the
573   validity of FEA results. Some types of simplification such as model 1 (one material) result
574   in smaller degrees of deformation, a 'stiffening of the cranium' (Figs. 2 and 8), while others
575   (e.g. inaccurate lateral nasal wall reconstruction in models 3 and 4) impact on both mode
576   and magnitude of deformation (Figs. 2 and 8). Previous work has shown that other
577   decisions in model construction, such as varying relative force magnitudes among jaw
578   closing muscles, impact on both mode of deformation and strain contours, while total
579   applied muscle force impacts more on magnitude of deformation and strains (Fitton et al,
580   2012).

581 This is important because it means that unless each model whose performance is to be
582 compared has been separately refined using specimen specific validation data there will
583 always be a degree of uncertainty concerning differences in mode and degree of
584 deformation which will impact strain contour maps, strain magnitudes and assessments of
585 global deformation. Such validation is difficult in extant and impossible in living humans
586 and fossil material.

587 However, through this and the many validation and sensitivity analyses cited above, we
588 know that some types of error (material properties, muscle force vector magnitudes,
589 simplifications in model geometry of certain types) will affect magnitude rather more than
590 mode of deformation. Further, other types of error (in e.g. relative muscle activation,
591 muscle force vector directions, simplifications in model geometry of certain types) will
592 impact more on mode than magnitude of deformation. Thus carefully designed
593 experiments that keep constant muscle vectors and relative activations and apply certain
594 simplifications of model geometry (that do not affect e.g. nasal wall anatomy) and use the
595 same degree of homogeneity and isotropy of material properties may produce reasonable
596 results with regard to mode but not magnitude of deformation. In such cases comparisons
597 should cautiously be based on relative strains within models or the direction components
598 of vectors of global deformation to minimise the risk of reaching erroneous conclusions.
599 The validity of such analyses will, however, depend on the validity of the assumption of
600 constant muscle load vectors and on how geometry has been simplified in each as well as
601 on the magnitude the biological signal (the true differences in performance) relative to the
602 magnitude of error. Much is yet to be learned through careful sensitivity and validation
603 studies before the impact of modelling and loading errors is fully understood and the field
604 can be confident that differences in model performance reflect biological reality.

605 It may be more secure to adopt an explicitly experimental approach to the application of
606 FEA to comparative cranial functional analyses, asking specific questions about the impact
607 of particular aspects of morphology on cranial performance. This approach maintains all
608 aspects of the model and loading constant except for the feature of interest (e.g. sutures,
609 periodontal ligament; Moazen et al. 2009; Wood et al. 2011; Wang et al. 2012) which is
610 modified and the impact on performance assessed.

611 The present study was limited by several factors. Significant but, we believe adequately
612 corrected for (see methods), is the issue of comparing surface strains projected onto a
613 plane (DSPI output) with predicted strains over a 3D surface. Beyond this, the use of a

614   single cadaveric specimen, does not allow us to assess variation in the validity of outputs
615   over a range of different morphologies. This is a limitation that is imposed by the
616   complexity of obtaining human material for such work and the effort and resources
617   required to carry out the detailed experimental and subsequent modelling work. Uniquely,
618   in the present study we are able to present comprehensive sensitivity and validation using a
619   single specimen and the largest and most directly measured map of surface strains to date.
620   The findings indicate that a fairly simple model (model 5) is able to replicate the mode and
621   magnitude of deformation of the physical cranium. However, the several sources of error
622   in model building have different degrees of impact on mode and magnitude of deformation
623   and hence, on the strain contours and magnitudes. This calls for great care in the
624   application of FEA in the wider, comparative context. Finally, all of the considerations we
625   raise in this paper with regard to error in comparison of cranial performance are likely to
626   also apply to greater or lesser degree to other skeletal elements.

627

628

Conclusion

629

630 By comparing the strains predicted by a series of FE models of the human cranium with
631 those measured *in vitro* in the actual specimen, the impacts of different modelling
632 simplifications on predicted deformations were assessed. The hypothesis that there are no
633 differences in strains predicted by the FE models and those measured in the cranium was
634 falsified. Thus, the performance of all models differed to some degree from that of the
635 experimentally loaded cranium. However, even though the model built with only cortical
636 bone and teeth as distinct materials showed strain magnitudes that were about 3.5 times
637 lower than the experimentally loaded cranium, the mode of deformation was very similar.
638 Omitting internal sinus and nasal walls led to alterations in both modes and magnitudes of
639 deformation.

640 The second hypothesis, that there are no differences in magnitudes and modes of
641 deformation among finite element models of the same skull built using different
642 approaches, was falsified. Modes of deformation (as assessed by strain vectors, contour
643 plots and a size and shape analysis) are less sensitive to how cancellous bone is represented
644 and to variations in model resolution, over the limited range examined here, than to
645 variations in sinus and nasal wall representation. Thus, simplifications of cancellous bone
646 anatomy have an impact on magnitude rather than mode of deformation while under-
647 representation of very thin bony structures such as are found in the sinus and nasal walls
648 impacts on both mode and magnitude of deformation. These differences suggest that
649 comparative FEA studies of biting performance among crania will likely suffer from error,
650 due to uncertainty in the modelling process. The extent to which this error limits our ability
651 to make ecological inferences from crania is likely significant but requires thorough
652 investigation.

653

Acknowledgements

654

661   **Authors' contributions**

662   VT-I, LCF and PO'H: study conception and design. VT-I: FE model construction. VT-I

663   and PO'H: DSPI and FE data analysis. VT-I, LCF, MJF and PO'H: DSPI experiments,

664   interpretation of results and manuscript writing.

665

References

Barak MM, Geiger S, Chattah NL-T, Shahar R, Weiner S (2009) Enamel dictates whole tooth deformation: A finite element model study validated by a metrology method. *J Struct Biol,* **168,** 511-520.

Benazzi S, Kullmer O, Grosse IR, Weber GW (2012) Brief communication: Comparing loading scenarios in lower first molar supporting bone structure using 3d finite element analysis. *Am J Phys Anthropol,* **147,** 128-134.

Berthaume MA, Dechow PC, Iriarte-Diaz J, et al. (2012) Probabilistic finite element analysis of a craniofacial finite element model. *J Theor Biol,* **300,** 242-253.

Bright JA (2012) The importance of craniofacial sutures in biomechanical finite element models of the domestic pig. *PLoS ONE,* **7,** e31769.

Bright JA, Gröning F (2011) Strain accommodation in the zygomatic arch of the pig: A validation study using digital speckle pattern interferometry and finite element analysis. *J Morphol,* **272,** 1388-1398.

Cox PG, Rinderknecht A, Blanco RE (2015) Predicting bite force and cranial biomechanics in the largest fossil rodent using finite element analysis. *J Anat,* **226,** 215-223.

Curtis N, Witzel U, Fitton LC, O'higgins P, Fagan MJ (2011) The mechanical significance of the temporal fasciae in *macaca fascicularis*: An investigation using finite element analysis. *Anat Rec,* **294,** 1178-1190.

Chamoli U, Wroe S (2011) Allometry in the distribution of material properties and geometry of the felid skull: Why larger species may need to change and how they may achieve it. *J Theor Biol,* **283,** 217-226.

Daegling DJ, Granatosky MC, McGraw WS (2015) Spatial patterning of bone stiffness in the anterior mandibular corpus of macaca fascicularis: Implications for models of bone adaptation. *Am J Phys Anthropol,* **156,** 649-660.

Dechow PC, Nail GA, Schwartz-Dabney CL, Ashman RB (1993) Elastic properties of human supraorbital and mandibular bone. *Am J Phys Anthropol,* **90,** 291-306.

Fagan MJ, Curtis N, Dobson CA, et al. (2007) Voxel-based finite analysis - working directly with microct scan data. *J Morphol,* **268,** 1071.

Fitton LC, Prôa M, Rowland C, Toro-Ibacache V, O'Higgins P (2015) The impact of simplifications on the performance of a finite element model of a *macaca fascicularis* cranium. *Anat Rec,* **298,** 107-121.

698   **Fitton LC, Shi JF, Fagan MJ, O'Higgins P** (2012) Masticatory loadings and cranial

699   deformation in *macaca fascicularis*: A finite element analysis sensitivity study. *J Anat,* **221,** 55-

700   68.

701   **Gröning F, Fagan M, O'Higgins P** (2011a) The effects of the periodontal ligament on

702   mandibular stiffness: A study combining finite element analysis and geometric

703   morphometrics. *J Biomech,* **44,** 1304-1312.

704   **Gröning F, Fagan MJ, O'Higgins P** (2012) Modeling the human mandible under

705   masticatory loads: Which input variables are important? *Anat Rec,* **295,** 853-863.

706   **Gröning F, Liu J, Fagan MJ, O'Higgins P** (2011b) Why do humans have chins? Testing

707   the mechanical significance of modern human symphyseal morphology with finite element

708   analysis. *Am J Phys Anthropol,* **144,** 593-606.

709   **Gröning F, Liu J, Fagan MJ, O'Higgins P** (2009) Validating a voxel-based finite

710   element model of a human mandible using digital speckle pattern interferometry. *J Biomech,*

711   **42,** 1224-1229.

712   **Gross MD, Arbel G, Hershkovitz I** (2001) Three-dimensional finite element analysis of

713   the facial skeleton on simulated occlusal loading. *J Oral Rehabil,* **28,** 684-694.

714   **Horgan T, Gilchrist M** (2003) The creation of three-dimensional finite element models

715   for simulating head impact biomechanics. *Int J Crashworthiness,* **8,** 353-366.

716   **Jansen van Rensburg GJ, Wilke DN, Kok S** (2012) Human skull shape and masticatory

717   induced stress: Objective comparison through the use of non‐rigid registration. *Int J Numer*

718   *Method Biomed Eng,* **28,** 170–185.

719   **Keyak J, Meagher J, Skinner H, Mote C** (1990) Automated three-dimensional finite

720   element modelling of bone: A new method. *J Biomed Eng,* **12,** 389-397.

721   **Kupczik K, Dobson CA, Crompton RH, et al.** (2009) Masticatory loading and bone

722   adaptation in the supraorbital torus of developing macaques. *Am J Phys Anthropol,* **139,** 193-

723   203.

724   **Kupczik K, Dobson CA, Fagan MJ, Crompton RH, Oxnard CE, O'Higgins P** (2007)

725   Assessing mechanical function of the zygomatic region in macaques: Validation and

726   sensitivity testing of finite element models. *J Anat,* **210,** 41-53.

727   **Lengsfeld M, Schmitt J, Alter P, Kaminsky J, Leppek R** (1998) Comparison of

728   geometry-based and ct voxel-based finite element modelling and experimental validation.

729   *Med Eng Phys,* **20,** 515-522.

730   **Lieberman DE** (1996) How and why humans grow thin skulls: Experimental evidence for

731   systemic cortical robusticity. *Am J Phys Anthropol,* **101,** 217-236.

732 **Liu J, Shi J, Fitton LC, Phillips R, O'Higgins P, Fagan MJ** (2012) The application of
733 muscle wrapping to voxel-based finite element models of skeletal structures. *Biomech Model*
734 *Mechan,* **11,** 35-47.

735 **Marinescu R, Daegling DJ, Rapoff AJ** (2005) Finite-element modeling of the
736 anthropoid mandible: The effects of altered boundary conditions. *Anat Rec A Discov Mol*
737 *Cell Evol Biol,* **283,** 300-309.

738 **McElhaney JH, Fogle JL, Melvin JW, Haynes RR, Roberts VL, Alem NM** (1970)
739 Mechanical properties of cranial bone. *J Biomech,* **3,** 495-511.

740 **Menegaz RA, Sublett SV, Figueroa SD, Hoffman TJ, Ravosa MJ, Aldridge K** (2010)
741 Evidence for the influence of diet on cranial form and robusticity. *Anat Rec,* **293,** 630-641.

742 **Meredith N, Sherriff M, Setchell D, Swanson S** (1996) Measurement of the
743 microhardness and young's modulus of human enamel and dentine using an indentation
744 technique. *Arch Oral Biol,* **41,** 539-545.

745 **Milne N, O'Higgins P** (2012) Scaling of form and function in the xenarthran femur: A
746 100-fold increase in body mass is mitigated by repositioning of the third trochanter. *Proc R*
747 *Soc B,* **279,** 3449-3456.

748 **Misch CE, Qu Z, Bidez MW** (1999) Mechanical properties of trabecular bone in the
749 human mandible: Implications for dental implant treatment planning and surgical
750 placement. *J Oral Maxillofac Surg,* **57,** 700-706.

751 **Moazen M, Curtis N, O'Higgins P, Jones MEH, Evans SE, Fagan MJ** (2009)
752 *Assessment of the role of sutures in a lizard skull: A computer modelling study.*

753 **Moss ML** (2007) The differential roles of periosteal and capsular functional matrices in
754 orofacial growth. *Eur J Orhod,* **29,** i96-i101.

755 **O'Higgins P, Cobb SN, Fitton LC, et al.** (2011) Combining geometric morphometrics
756 and functional simulation: An emerging toolkit for virtual functional analyses. *J Anat,* **218,**
757 3-15.

758 **O'Higgins P, Fitton LC, Phillips R, et al.** (2012) Virtual functional morphology: Novel
759 approaches to the study of craniofacial form and function. *Evol Biol,* **39,** 521-535.

760 **O'Higgins P, Milne N** (2013) Applying geometric morphometrics to compare changes in
761 size and shape arising from finite elements analyses. *Hystrix,* **24,** 126-132.

762 **Olesiak SE, Sponheimer M, Eberle JJ, Oyen ML, Ferguson VL** (2010)
763 Nanomechanical properties of modern and fossil bone. *Palaeogeography, Palaeoclimatology,*
764 *Palaeoecology,* **289,** 25-32.

765 **Peterson J, Dechow PC** (2003) Material properties of the human cranial vault and
766 zygoma. *Anat Rec,* **274A,** 785-797.

767 **Rayfield EJ** (2007) Finite element analysis and understanding the biomechanics and
768 evolution of living and fossil organisms. *Annu Rev Earth Planet Sci,* **35,** 541-576.

769 **Renders G, Mulder L, Van Ruijven L, Langenbach G, Van Eijden T** (2011) Mineral
770 heterogeneity affects predictions of intratrabecular stress and strain. *J Biomech,* **44,** 402-407.

771 **Ross CF, Berthaume MA, Dechow PC, et al.** (2011) *In vivo* bone strain and finite-
772 element modeling of the craniofacial haft in catarrhine primates. *J Anat,* **218,** 112-141.

773 **Schwartz-Dabney CL, Dechow PC** (2003) Variations in cortical material properties
774 throughout the human dentate mandible. *Am J Phys Anthropol,* **120,** 252-277.

775 **Smith AL, Benazzi S, Ledogar JA, et al.** (2015a) Biomechanical implications of
776 intraspecific shape variation in chimpanzee crania: Moving toward an integration of
777 geometric morphometrics and finite element analysis. *Anat Rec,* **298,** 122-144.

778 **Smith AL, Benazzi S, Ledogar JA, et al.** (2015b) The feeding biomechanics and dietary
779 ecology of *paranthropus boisei. Anat Rec,* **298,** 145-167.

780 **Strait DS, Wang Q, Dechow PC, et al.** (2005) Modeling elastic properties in finite-
781 element analysis: How much precision is needed to produce an accurate model? *Anat Rec,*
782 **283,** 275-287.

783 **Strait DS, Weber GW, Neubauer S, et al.** (2009) The feeding biomechanics and dietary
784 ecology of *australopithecus africanus. PNAS,* **106,** 2124-2129.

785 **Szwedowski TD, Fialkov J, Whyne CM** (2011) Sensitivity analysis of a validated subject-
786 specific finite element model of the human craniofacial skeleton. *Proc Inst Mech Eng H J*
787 *Eng,* **225,** 58-67.

788 **Toro-Ibacache V, Zapata Muñoz V, O'Higgins P** (2015) The relationship between
789 skull morphology, masticatory muscle force and cranial skeletal deformation during biting.
790 *Ann Anat,* DOI: 10.1016/j.aanat.2015.03.002.

791 **Truesdell C, Noll W** (2004) *The non-linear field theories of mechanics,* Springer, Berlin.

792 **Turner-Walker G, Parry TV** (1995) The tensile strength of archaeological bone. *Journal of*
793 *Archaeological Science,* **22,** 185-191.

794 **Wang Q, Wood SA, Grosse IR, et al.** (2012) The role of the sutures in biomechanical
795 dynamic simulation of a macaque cranial finite element model: Implications for the
796 evolution of craniofacial form. *Anat Rec.*

797 **Wood SA, Strait DS, Dumont ER, Ross CF, Grosse IR** (2011) The effects of modeling

798 simplifications on craniofacial finite element models: The alveoli (tooth sockets) and

799 periodontal ligaments. *J Biomech,* **44,** 1831-1838.

800 **Wroe S, Ferrara TL, McHenry CR, Curnoe D, Chamoli U** (2010) The

801 craniomandibular mechanics of being human. *Proc R Soc B,* **277,** 3579-3586.

802 **Yang L, Ettemeyer A** (2003) Strain measurement by three-dimensional electronic speckle

803 pattern interferometry: Potentials, limitations, and applications. *Opt Eng,* **42,** 1257-1266.

804 **Yang L, Zhang P, Liu S, Samala PR, Su M, Yokota H** (2007) Measurement of strain

805 distributions in mouse femora with 3d-digital speckle pattern interferometry. *Opt Las Eng,*

806 **45,** 843-851.

807

808

809

810 **Tables**

811 **Table 1.** Characteristics of the finite element models. Young's modulus: Bone=17

812 GPa; cortical bone=17 GPa; cancellous bone=56 MPa; teeth=50 GPa.

Model	Voxel size (mm)	No. of elements	Materials	Material volume		Features
				mm³	%	
Model 1	0.48 x 0.48 x 0.48	4,028,280	Bone (cortical+cancellous)	448,472.94	97.96	Full manual reconstruction of sinus bony walls.
			Teeth	9,316.41	2.04	
Model 2	0.48 x 0.48 x 0.48	3,326,922	Cortical bone	327,851.44	86.71	Partial (threshold based) reconstruction of inner sinus bony walls.
			Cancellous bone	40,916.34	10.82	
			Teeth	9,316.53	2.46	
Model 3	0.48 x 0.48 x 0.48	3,504,595	Cortical bone	347,999.16	87.38	Full manual reconstruction of sinus bony walls.
			Cancellous bone	40,960.09	10.28	
			Teeth	9,316.53	2.34	
Model 4	0.35 x 0.35 x 0.35	8,817,889	Cortical bone	327,113.15	86.74	Like model 2.
			Cancellous bone	40,734.59	10.80	
			Teeth	9,284.42	2.46	
Model 5	0.35 x 0.35 x 0.35	9,241,525	Cortical bone	345,217.06	87.34	Like model 3.
			Cancellous bone	40,749.30	10.31	
			Teeth	9,284.29	2.35	

813

814

815 **Table 2.** Correlation of strain magnitudes between the most detailed model (5) and the

816 other models.

		Linear correlations (r)			
Model 5	Principal strains	Model 1	Model 2	Model 3	Model 4
Line 1	ε1	0.91	0.83	0.97	0.90
	ε3	0.91	0.93	0.98	0.97
Line 2	ε1	0.98	0.96	0.97	0.99
	ε3	0.96	0.97	0.98	0.99
Line 3	ε1	0.80	0.71	0.88	0.75
	ε3	0.85	0.81	0.90	0.73
Line 4	ε1	0.85	0.25	0.85	0.36
	ε3	0.87	0.36	0.87	0.34

817

818

819 **Figure Legends**

820 **Fig. 1.** Experimental setup for *in vitro* strain measurement. (a) Vertical compressive load

821 applied to the calvarium (upper arrow) simulating a left central incisor bite (lower arrow).

822 The asterisk shows the DSPI sensor attached to the infraorbital region. (b) DSPI-based

823 surface strain measurement, where the unstrained surface (upper image) provides a speckle

824 interferogram that changes under load. The change is quantified in a phase map (middle

825 image). Surface strains are calculated from 3D displacements, and expressed as colour-

826 coded strain contour plots and strain vector orientations (lower image). The position of the

827 nose is shown for reference.

828 **Fig. 2.** Cranium and finite element models. (a) Coronal section of the CT (Cranium) and

829 the five FE models showing the results produced by different segmentations; green

830 represents cortical bone, red represents cancellous bone and white represents teeth. (b)

831 Cranium with overlaid DSPI results, and FE models showing maximum principal strain ε_1

832 (upper row) and minimum principal strain ε_3 (lower row) strain contour plots. (c) Adjusted

833 ranges of ε_1 (upper row) and ε_3 (lower row) contour plots for models 1, 3 and 5 to match

834 the strain distributions of DSPI on the cranium, and models 2 and 4.

835 **Fig. 3.** Lines for extracting strain magnitudes and landmarks for size and shape analysis. (a)

836 Landmark lines on the FE model surface. (b) Corresponding lines in the DSPI outputs. (c)

837 Landmarks for Procrustes size and shape analysis.

838 **Fig. 4.** *In vitro* vs. predicted strain magnitudes across the infraorbital region. The grey area

839 represents the mean measured (DSPI) strains $\pm$ 2 standard deviations (SD). The strain

840 magnitudes predicted for model 1 multiplied by 3.5 were also plotted; this approximately

841 corrects for increased model stiffness due to infilled cancellous bone.

842 **Fig. 5.** *In vitro* vs. predicted strain magnitudes across the frontal process of the maxilla. The

843 grey area represents the mean measured (DSPI) strains $\pm$ 2 standard deviations (SD). The

844 strain magnitudes predicted for model 1 multiplied by 3.5 were also plotted; this

845 approximately corrects for increased model stiffness due to infilled cancellous bone.

846 **Fig. 6.** *In vitro* vs. predicted directions of strains in the infraorbital region. Black lines

847 represent the vectors of strains in 2D (DSPI) and 3D (FE models). (a) maximum principal

848 strain ε_1 and (b) minimum principal strain ε_3. To best match contours and to facilitate the

849 identification of corresponding regions, vector magnitudes in the FEA outputs and ranges

850 of each strain contour plot have been independently adjusted.

851   **Fig. 7.** *In vitro* vs. predicted directions of strains in the frontal process of the maxilla. Black

852   lines represent the vectors of strains in 2D (DSPI) and 3D (FE models). (a) Maximum

853   principal strain ε_1 and (b) minimum principal strain ε_3. To best match contours and to

854   facilitate the identification of corresponding regions, vector magnitudes in the FEA outputs

855   and ranges of each strain contour plot have been independently adjusted.

856   **Fig. 8.** Principal components analysis of size and shape variables based on 51 landmarks

857   representing deformation of models 1 to 5 under a simulated incisor bite respect to the

858   unloaded cranium. Deformations are magnified 250 times to facilitate visualisation.
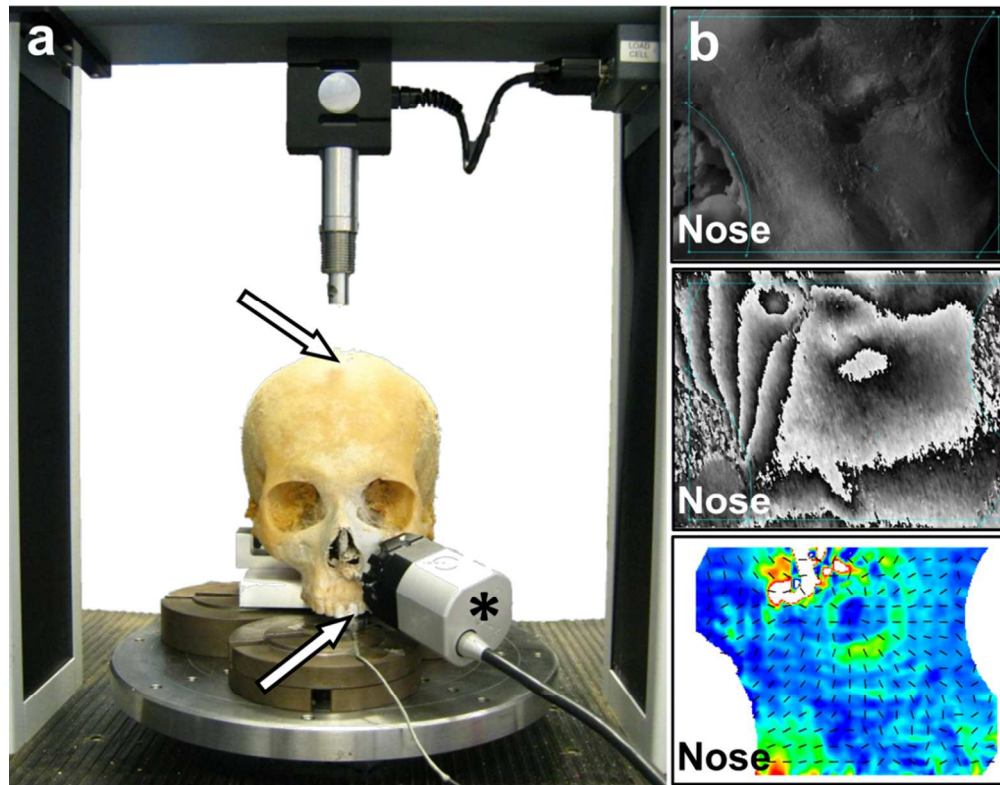
Fig. 1. Experimental setup for in vitro strain measurement. (a) Vertical compressive load applied to the calvarium (upper arrow) simulating a left central incisor bite (lower arrow). The asterisk shows the DSPI sensor attached to the infraorbital region. (b) DSPI-based surface strain measurement, where the unstrained surface (upper image) provides a speckle interferogram that changes under load. The change is quantified in a phase map (middle image). Surface strains are calculated from 3D displacements, and expressed as colour-coded strain contour plots and strain vector orientations (lower image). The position of the nose is shown for reference.
90x70mm (300 x 300 DPI)
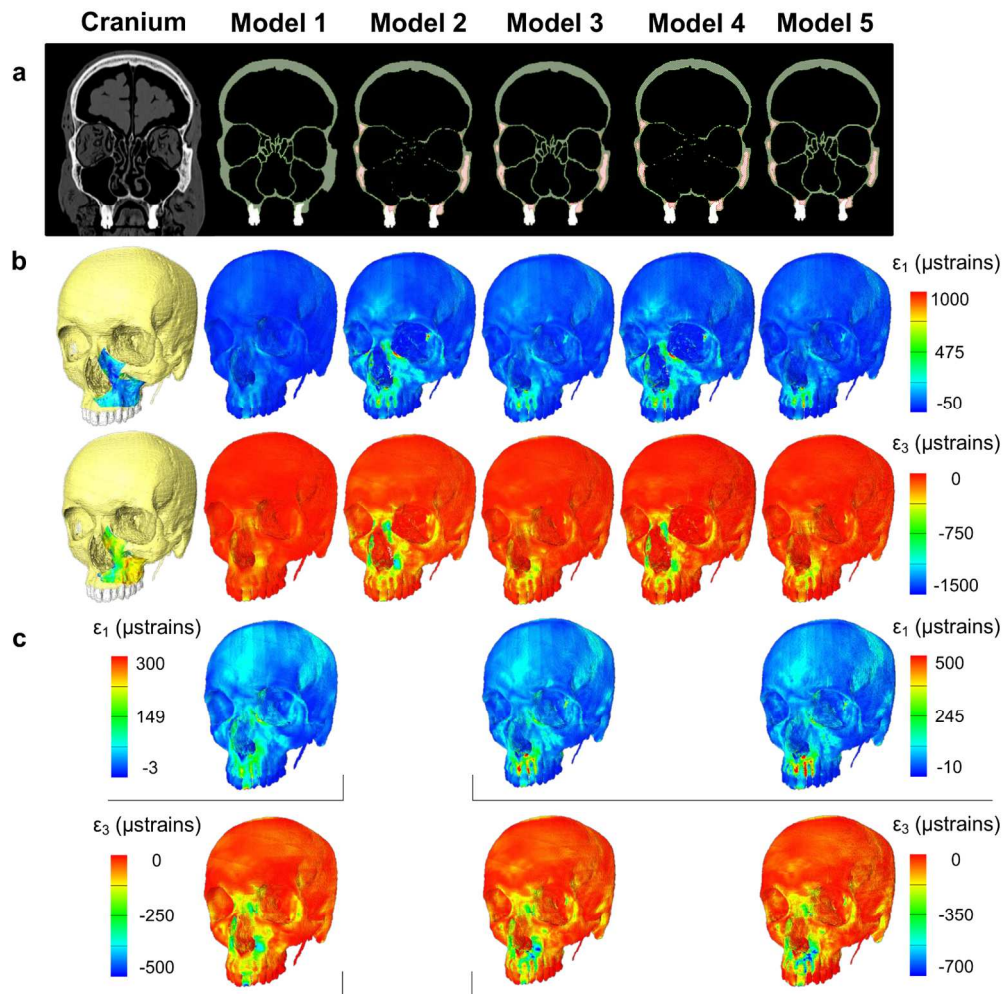
Fig. 2. Cranium and finite element models. (a) Coronal section of the CT (Cranium) and the five FE models showing the results produced by different segmentations; green represents cortical bone, red represents cancellous bone and white represents teeth. (b) Cranium with overlaid DSPI results, and FE models showing maximum principal strain ε1 (upper row) and minimum principal strain ε3 (lower row) strain contour plots. (c) Adjusted ranges of ε1 (upper row) and ε3 (lower row) contour plots for models 1, 3 and 5 to match the strain distributions of DSPI on the cranium, and models 2 and 4.
145x146mm (300 x 300 DPI)
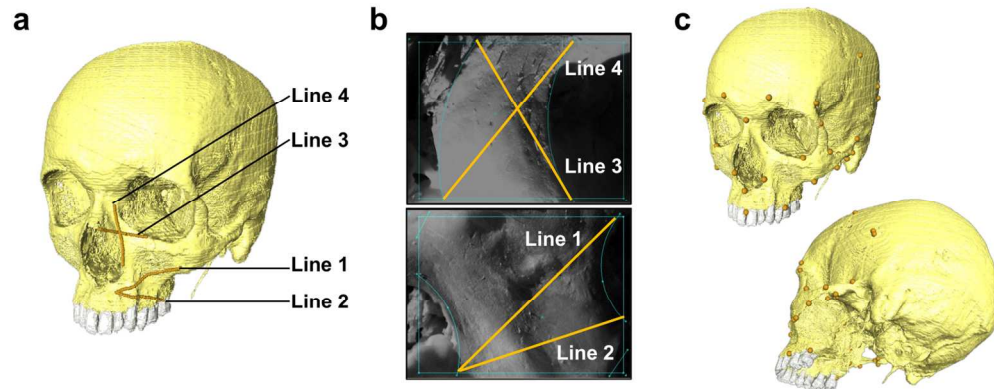
Fig. 3. Lines for extracting strain magnitudes and landmarks for size and shape analysis. (a) Landmark lines on the FE model surface. (b) Corresponding lines in the DSPI outputs. (c) Landmarks for Procrustes size and shape analysis.
150x59mm (300 x 300 DPI)
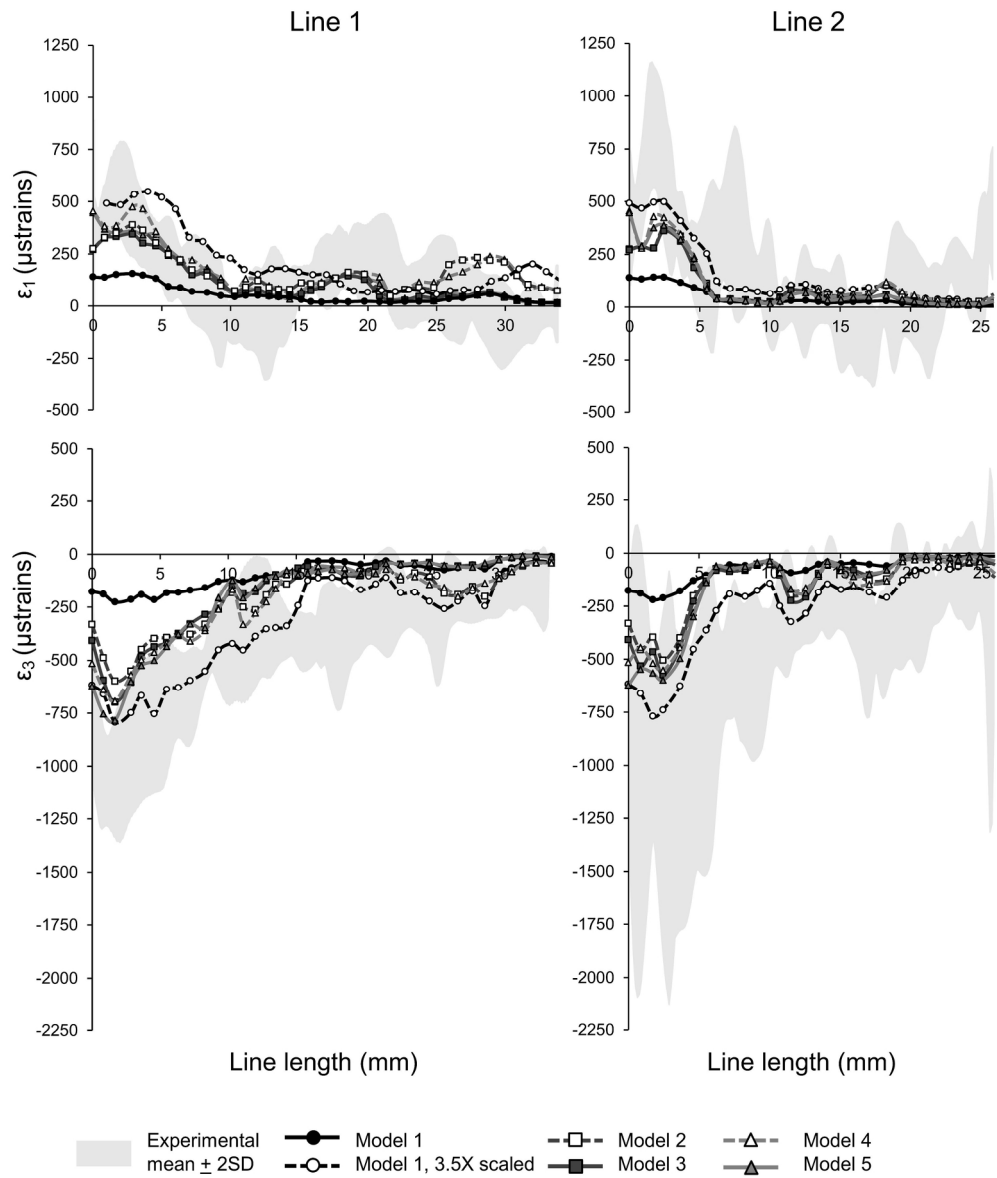
Fig. 4. In vitro vs. predicted strain magnitudes across the infraorbital region. The grey area represents the mean measured (DSPI) strains + 2 standard deviations (SD). The strain magnitudes predicted for model 1 multiplied by 3.5 were also plotted; this approximately corrects for increased model stiffness due to infilled cancellous bone.
191x229mm (300 x 300 DPI)
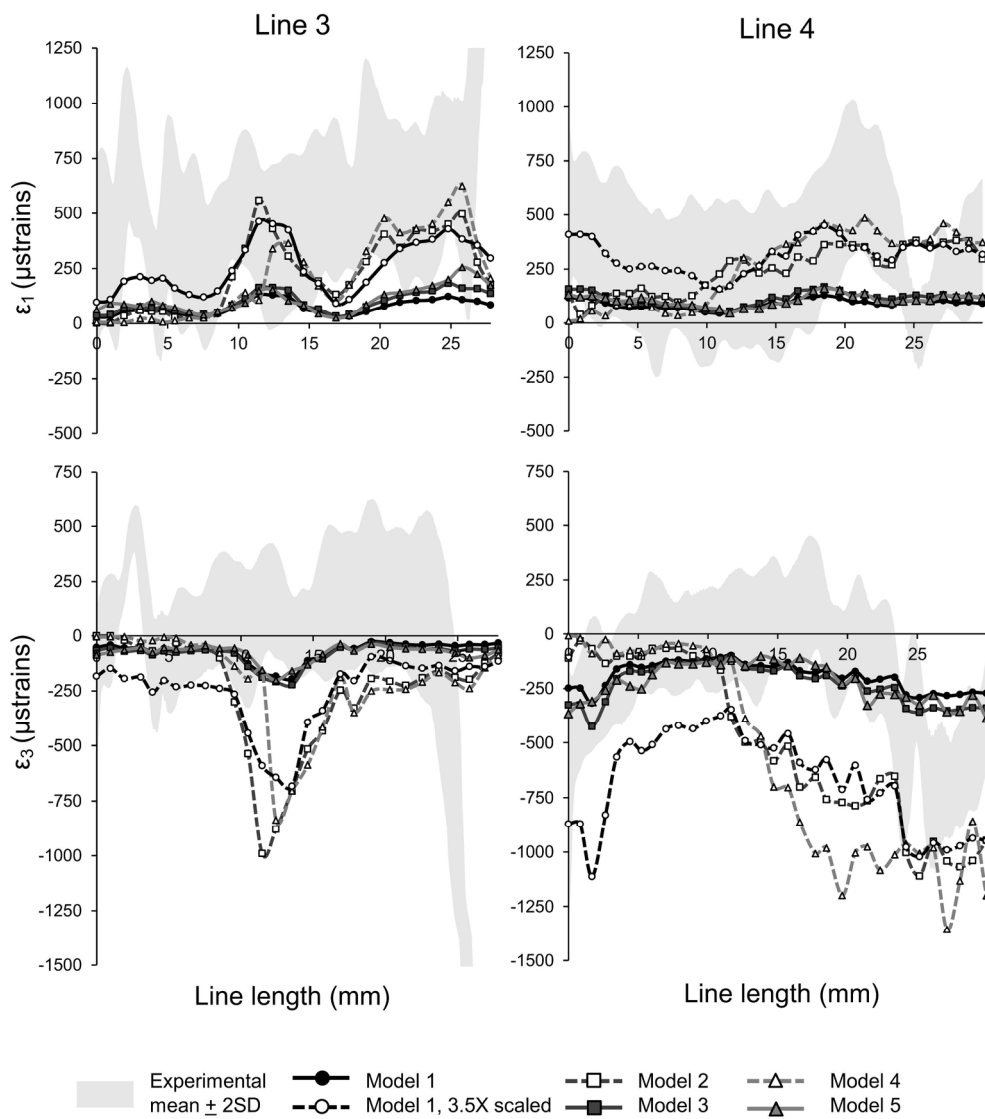
Fig. 5. In vitro vs. predicted strain magnitudes across the frontal process of the maxilla. The grey area represents the mean measured (DSPI) strains + 2 standard deviations (SD). The strain magnitudes predicted for model 1 multiplied by 3.5 were also plotted; this approximately corrects for increased model stiffness due to infilled cancellous bone.
174x197mm (300 x 300 DPI)
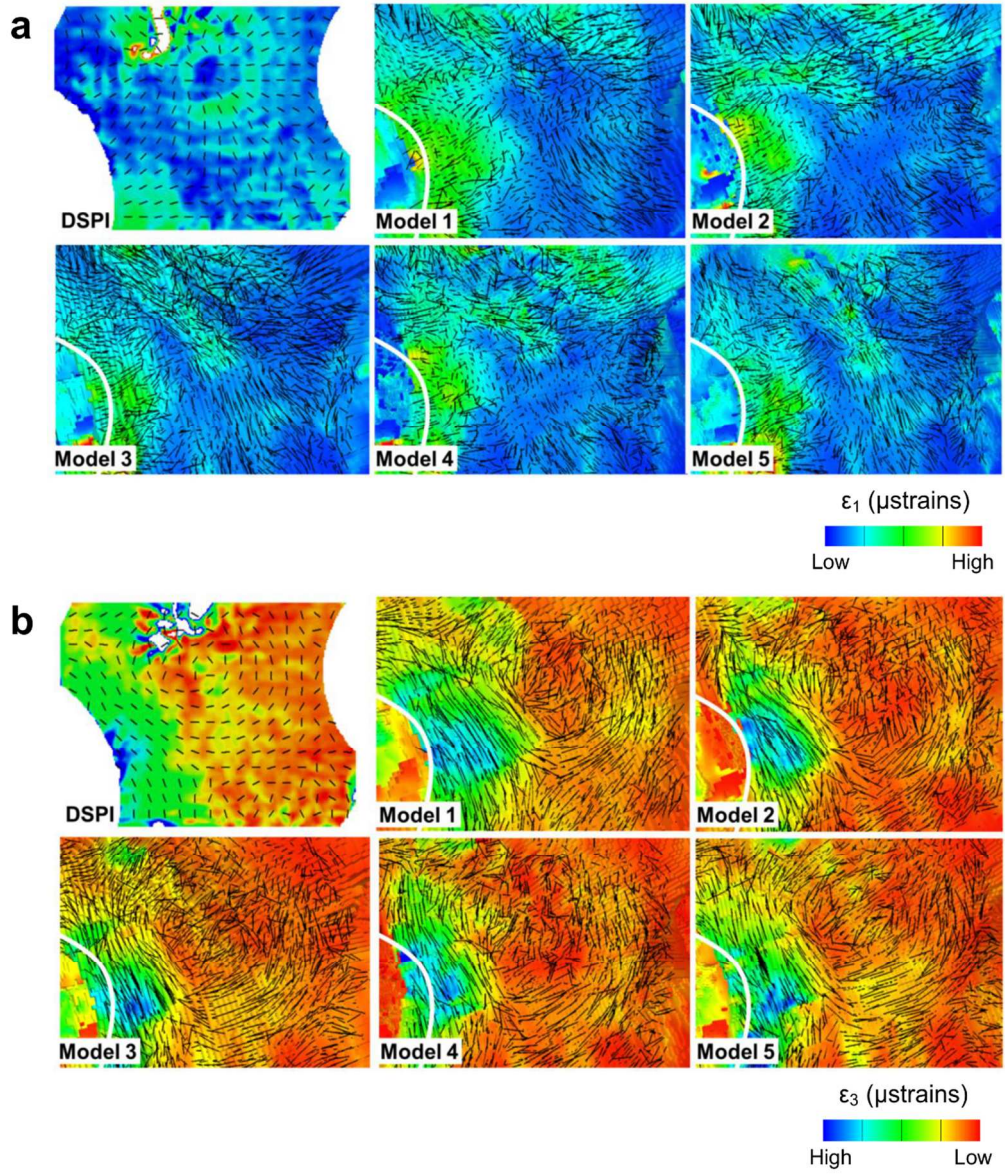
Fig. 6. In vitro vs. predicted directions of strains in the infraorbital region. Black lines represent the vectors of strains in 2D (DSPI) and 3D (FE models). (a) maximum principal strain ε1 and (b) minimum principal strain ε3. To best match contours and to facilitate the identification of corresponding regions, vector magnitudes in the FEA outputs and ranges of each strain contour plot have been independently adjusted. 110x130mm (300 x 300 DPI)
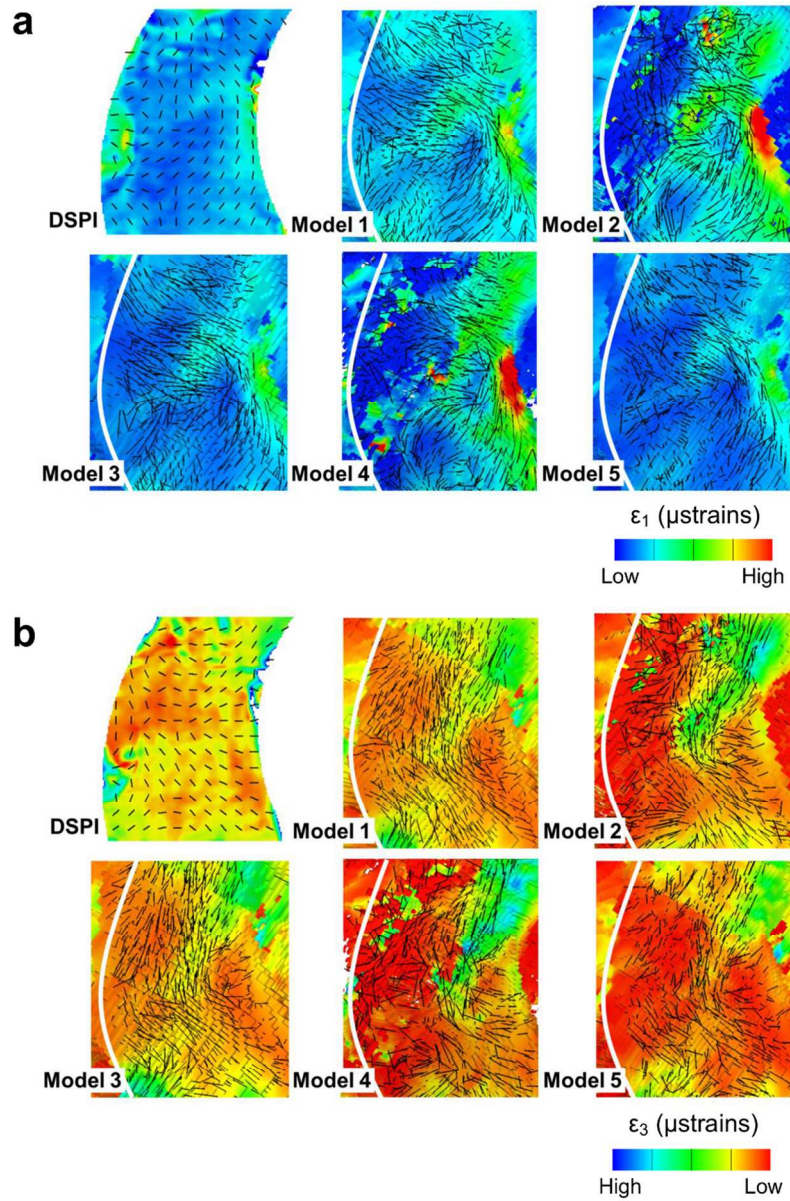
Fig. 7. In vitro vs. predicted directions of strains in the frontal process of the maxilla. Black lines represent the vectors of strains in 2D (DSPI) and 3D (FE models). (a) Maximum principal strain ε1 and (b) minimum principal strain ε3. To best match contours and to facilitate the identification of corresponding regions, vector magnitudes in the FEA outputs and ranges of each strain contour plot have been independently adjusted.

87x131mm (300 x 300 DPI)
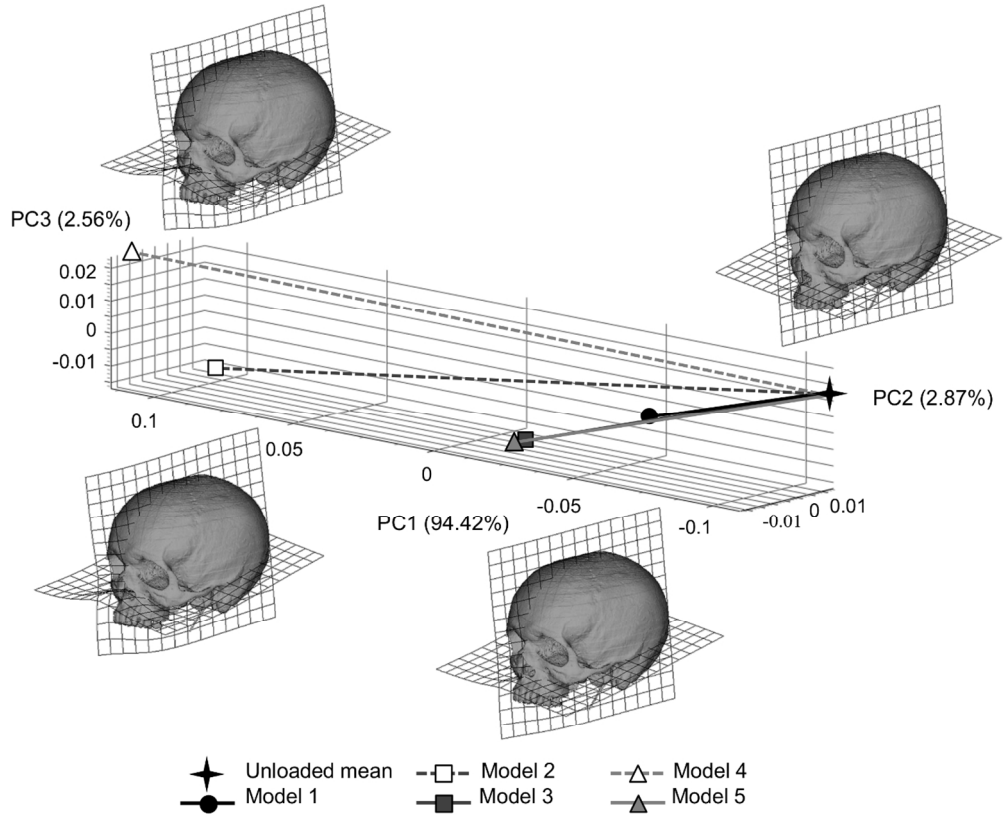
Fig. 8. Principal components analysis of size and shape variables based on 51 landmarks representing deformation of models 1 to 5 under a simulated incisor bite respect to the unloaded cranium. Deformations are magnified 250 times to facilitate visualisation.
119x98mm (300 x 300 DPI)

Supporting Information

Table 1. Landmarks for Procrustes size and shape analysis.

No.	Definition
1	Vertex - highest point of the cranial vault.
2	Nasion - intersection between frontonasal and internasal suture.
3	Anterior nasal spine - tip of the anterior nasal spine.
4	Prosthion - most buccal and occlusal point of the interalveolar septum between central incisors.
5	Occiput - most posterior point of the neurocranium.
6&20	Supraorbital torus - most anterior point of supraorbital ridge.
7&21	Infraorbitale - most inferior point of the infraorbital ridge.
8&22	Nasal notch - most lateral part of the nasal aperture.
9&23	First molar - most buccal and mesial point of the junction of the M1 and alveolar process. If M1 is absent, the landmark is in the lowest most buccal point of the interalveolar septum between the second premolar and the next present molar.
10&24	Last molar – most buccal and distal point of the junction between the last molar and the alveolar process.
11&25	Zygo-maxillar - most inferior point of the zygo-maxillary junction.
12&26	Fronto-zygomatic - most lateral point of the fronto-zygomatic junction.
13&27	Fronto-temporal angle - point of intersection between the frontal and temporal processes of the zygomatic bone.
14&28	Zygomatic arch lateral - most lateral point of the zygomatic arch.
15&29	Zygomatic root posterior - most posterior-superior point of the intersection zygomatic root and the squama of the temporal bone.
16&30	Zygomatic root anterior - most anterior point of the intersection between the zygomatic root and the squama of the temporal bone.
17&31	Zygomatic arch medial - most lateral point on the inner face of the zygomatic arch.
18&32	Infratemporal crest - most medial point of the infratemporal crest.
19&33	Eurion - most lateral point of the neurocranium.
34&37	Anterior temporal - most anterior point of the origin of the temporal muscle in the temporal line.
35&38	Superior temporal - most superior point of the origin of the temporal muscle in the temporal line.
36&39	Posterior temporal - most posterior point of the origin of the temporal muscle in the temporal line.
40&43	Anterior masseter - most anterior point of the origin of the masseter muscle in the zygomatic arch.
41&44	Posterior masseter - most posterior point of the origin of the masseter muscle in the zygomatic arch.
42&45	Mid-masseter - midpoint along the origin area of the masseter muscle in the zygomatic arch.
46&49	Superior pterygoid - most superior point of the origin of medial pterygoid muscle in the pterygoid fossa.
47&50	Inferior pterygoid - most inferior point of the origin of medial pterygoid muscle in the pterygoid fossa.
48&51	Mid-pterygoid - midpoint along the origin area of the medial pterygoid muscle in the pterygoid fossa.